

**DETERMINATION OF FLAME CHARACTERISTICS IN  
A LOW SWIRL BURNER AT GAS TURBINE  
CONDITIONS THROUGH REACTION ZONE IMAGING**

A Dissertation  
Presented to  
The Academic Faculty

by

Karthik Periagaram

In Partial Fulfillment  
of the Requirements for the Degree  
Doctor of Philosophy in the  
Guggenheim School of Aerospace Engineering

Georgia Institute of Technology  
December 2012

# TABLE OF CONTENTS

<b>List of Figures</b>	<b>iv</b>
<b>List of Tables</b>	<b>v</b>
<b>List of Symbols</b>	<b>vi</b>
<b>Summary</b>	<b>vii</b>
<b>1 Introduction</b>	<b>1</b>
1.1 Motivation . . . . .	1
<b>2 Background</b>	<b>2</b>
2.1 LSB flow field . . . . .	2
2.2 LSB flame stabilization . . . . .	2
2.3 CH PLIF Physical Process . . . . .	2
2.4 CH PLIF Signal Modeling . . . . .	3
2.5 Linearity . . . . .	3
2.6 CH PLIF Quenching Model . . . . .	4
<b>3 Experimental Methods and Considerations</b>	<b>12</b>
3.1 LSB configurations . . . . .	12
3.1.1 Configuration A . . . . .	12
3.1.1.1 Test Facility . . . . .	13
3.1.1.2 Low Swirl Burner . . . . .	15
3.1.2 Configuration B . . . . .	16
3.1.2.1 Test Facility . . . . .	18
3.1.2.2 Low Swirl Burner . . . . .	19

3.2	Diagnostics . . . . .	21
3.2.1	Laser Doppler Velocimetry . . . . .	21
3.2.2	CH* chemiluminescence . . . . .	23
3.2.2.1	Image Processing . . . . .	24
3.2.3	CH Planar Laser-Induced Fluorescence . . . . .	27
3.2.3.1	Imaging system . . . . .	29
3.2.3.2	Laminar Flame setup . . . . .	29
3.2.3.3	Laser Wavelength Calibration . . . . .	29
<b>4</b>	<b>CH PLIF Signal Modeling and Validation</b>	<b>32</b>
4.1	CH PLIF Development/Preliminary Experiments . . . . .	32
4.1.1	Excitation scan . . . . .	32
4.1.2	Linearity test . . . . .	34
4.2	Fluorescence Signal Modeling . . . . .	36
4.3	Results . . . . .	38
<b>5</b>	<b>LSB Flame Characteristics</b>	<b>39</b>
5.1	Effect of reference velocity . . . . .	39
5.2	Effect of preheat temperature . . . . .	41
5.3	Effect of swirler vane angle . . . . .	43
5.4	Effect of equivalence ratio . . . . .	44
5.5	Effect of combustor pressure . . . . .	45
5.6	Flame structure . . . . .	46
<b>6</b>	<b>Conclusions</b>	<b>47</b>
<b>A</b>	<b>Seeder Design</b>	<b>48</b>
	<b>References</b>	<b>52</b>

# LIST OF FIGURES

3.1	Schematic of Test Facility A . . . . .	14
3.2	Detail schematic of Configuration A . . . . .	16
3.3	Schematic of Test Facility B . . . . .	17
3.4	Detail schematic of Configuration B . . . . .	20
3.5	Schematic of the LDV setup . . . . .	22
3.6	Sample CH* Chemiluminescence data . . . . .	25
3.7	Schematic of the Alexandrite laser . . . . .	27
3.8	Schematic of the laser calibration experiment . . . . .	30
3.9	Laser wavelength calibration chart . . . . .	31
A.1	Schematic of the old seeder design . . . . .	49
A.2	Schematic of the new seeder design . . . . .	50

## LIST OF TABLES

2.1	Einstein A coefficients . . . . .	5
2.2	Quenching Cross-sections . . . . .	9
2.3	Einstein B coefficients . . . . .	10
2.4	Spectroscopic constants . . . . .	11
3.1	Swirler Dimensions . . . . .	13

## LIST OF SYMBOLS

$X_f$  Flame standoff distance

# SUMMARY

# CHAPTER 1

## INTRODUCTION

### 1.1 Motivation

The need to reduce pollutant emissions, particularly the oxides of nitrogen,  $\text{NO}_x$ , in order to meet increasingly stringent government regulations spurs efforts in the gas turbine industry to seek cleaner, more environment-friendly combustion concepts. The production rate of  $\text{NO}_x$  is highly temperature dependent and fuel-lean, premixed combustion is a widely employed technique to keep the adiabatic flame temperature under 1800 K. However, operating a combustor at such lean conditions results in eaker combustion processes that are highly susceptible to perturbations and combustor instabilities. This highlights the requirements for robust flame stabilization techniques to sustain combustion at ultra-lean conditions. The Low Swirl Burner (LSB) design addresses these requirements by providing a low  $\text{NO}_x$  combustor that can operate stably at lean equivalence ratios.



## CHAPTER 2 15

### BACKGROUND 16

#### 2.1 LSB flow field 17

#### 2.2 LSB flame stabilization 18

#### 2.3 CH PLIF Physical Process 19

CH is a minor species that is produced and destroyed by fast two-body reactions in the reaction zone of the flame. It is primarily produced by the break up of a hydrocarbon fuel and is known to play an important role in the formation of prompt  $\text{NO}_x$ . CH was the first radical to be detected in a flame by Laser Induced Fluorescence and was the second radical to be imaged by planar LIF. 20 21 22 23 24

The excitation scheme chosen for this study follows the work done by Li et al.[?] who used a similar laser system to excite the R-bandhead of the CH  $B^2\Sigma^- \leftarrow X^2\Pi$  (0,0) system. The scheme primarily targets CH molecules in the ground state with rotational quantum numbers between 5–9, in both the singlet and triplet states. Upon absorption, these molecules transition to the second electronically excited  $B$  state. At this point, the molecule has the following options; 25 26 27 28 29 30

1. The molecule can undergo spontaneous emission, release a photon and return to the ground state. 31 32
2. The molecule can undergo stimulated emission, release a photon and return to the ground state. 33 34
3. The molecule can collide elastically with other molecules and undergo relaxation in the vibrational/rotational modes. 35 36

4. The molecule can collide inelastically with other molecules in the system and gain or lose energy.

The lifetime of the excited  $B$  state, given by the reciprocal of the Einstein spontaneous emission coefficient, is long enough to allow for rotational relaxation through elastic collisions, but not long enough to allow for vibrational relaxation. Thus, the excited CH radicals are primarily confined to the  $B(0)$  state during the course of the LIF process.

The probability of the excited radicals undergoing stimulated emission is quite small. Why?

In the absence of any other physical process, these molecules would have undergone spontaneous de-excitation back to the ground state.

This primarily targets CH molecules with the rotational quantum numbers 5 through 9 in both the singlet and triplet states. These molecules

This populates the  $A^2\Delta$  state through fast electronic energy transfer from the  $B^2\Sigma^-$  state. The resulting broadband fluorescence observed between  $\lambda = 420\text{--}440$  nm is due to the  $A^2\Delta \rightarrow X^2\Pi$  (1,1),  $A^2\Delta \rightarrow X^2\Pi$  (0,0) and, to a lesser degree, from the  $B^2\Sigma^- \rightarrow X^2\Pi$  (0,1) bands.

## 2.4 CH PLIF Signal Modeling

## 2.5 Linearity

In the weak excitation limit, the signal is a function of CH concentration and the rate of collisional quenching of the excited CH radicals. In the strong excitation limit, the signal depends only on the CH concentration is unaffected by the quenching of the excited CH species.

It is difficult to ensure that the CH system is saturated spatially, temporally and spectrally at the same time. Further, operating with high laser intensities may bleach

the energy levels being excited by inducing chemical reactions that destroy the excited  
CH radicals. Hence, it is preferred to operate in the linear regime.

## 2.6 CH PLIF Quenching Model

In order to calculate the intensity of the quenched CH PLIF signal in a flame, an  
improved model of the CH system was constructed and analyzed. According to this  
new model, CH radicals from the  $X$  ground state are excited to the  $B(0)$  upper state.  
This is followed by collisional transfer to the  $A(1)$  and  $A(0)$  states. The transfer  
between the nearly degenerate  $A(1)$  and  $B(0)$  states is partially reversible. The  
transfer between  $B(0)$  and  $A(0)$  is not reversible. This is followed by spontaneous  
emission as CH radicals transition from the  $A$  states to the  $X$  state. This results in  
a pseudo-three-level model as shown in Figure FIXME.

Figure FIXME indicates the rates of the various processes discussed. The sub-  
scripts 0, 1 and 2 represent the electronic energy levels  $X$ ,  $A$  and  $B$  respectively.  
Processes involving the  $A(0)$  state are differentiated from those involving the  $A(1)$   
state by a prime ( $'$ ). With the exception of the nearly degenerate  $A(1)$  and  $B(0)$   
states, most collisional excitation steps are neglected due to their low probability.

In this formulation, the signal intensity of the CH PLIF emission is given by  
Equation 4.1.

$$S = (n_1 A_{10} + n'_1 A'_{10} + n_2 A_{20})V \quad (2.1)$$

The spontaneous emission coefficients,  $A_{10}$ ,  $A'_{10}$  and  $A_{20}$  are obtained from various  
published papers[1, 2, 3]. The values used for this analysis are presented in Table 2.1.

Equations 2.2-2.4 describe the time variation of the number density of CH radicals  
in each excited state.

Table 2.1: *The coefficients of spontaneous emission for transitions in the CH system are provided.*

Transition	Symbol	A, s <sup>-1</sup>
$B \rightarrow X(0, 0)$	$A_{20}$	$2.963 \times 10^6$
$A \rightarrow X(1, 1)$	$A_{10}$	$1.676 \times 10^6$
$A \rightarrow X(0, 0)$	$A'_{10}$	$1.832 \times 10^6$

$$\frac{dn_1}{dt} = -(A_{10} + Q_{10} + R_{12})n_1 + R_{21}n_2 \quad (2.2)$$

$$\frac{dn'_1}{dt} = -(A'_{10} + Q'_{10})n'_1 + R'_{21}n_2 \quad (2.3)$$

$$\frac{dn_2}{dt} = W_{02}n_0 + R_{12}n_1 - (A_{20} + Q_{20} + R_{21} + R'_{21})n_2 \quad (2.4)$$

At steady state, the rate of change of the number density is minimal. Under this assumption, the LHS of Equations 2.2–2.4 can be set to zero. This results in a closed set of linear equations in terms of the populations of the upper states. This set of equations is presented in Equation 2.5.

$$\begin{bmatrix} A_{10} + Q_{10} + R_{12} & 0 & -R_{21} \\ 0 & A'_{10} + Q'_{10} & -R'_{21} \\ -R_{12} & 0 & A_{20} + Q_{20} + R_{21} + R'_{21} \end{bmatrix} \begin{bmatrix} n_1 \\ n'_1 \\ n_2 \end{bmatrix} = \begin{bmatrix} 0 \\ 0 \\ W_{02}n_0 \end{bmatrix} \quad (2.5)$$

The solution to Equation 2.5 is shown in Equations 2.6–2.8.

$$n_1 = \frac{R_{21}}{(A_{10} + Q_{10} + R_{12})(A_{20} + Q_{20} + R_{21} + R'_{21}) - R_{12}R_{21}} W_{02}n_0 \quad (2.6)$$

$$n'_1 = \frac{(A_{10} + Q_{10} + R_{12})R'_{21}}{(A'_{10} + Q'_{10})((A_{10} + Q_{10} + R_{12})(A_{20} + Q_{20} + R_{21} + R'_{21}) - R_{12}R_{21})} W_{02}n_0 \quad (2.7)$$

$$n_2 = \frac{(A_{10} + Q_{10} + R_{12})}{(A_{10} + Q_{10} + R_{12})(A_{20} + Q_{20} + R_{21} + R'_{21}) - R_{12}R_{21}} W_{02}n_0 \quad (2.8)$$

These expressions can be further simplified by noting various observations made 89  
in studies of the CH system. For instance, previous work[4, 5] has reported that the 90  
*B* state is slightly (about 1.3 times) more prone to quenching compared to the *A* 91  
state. We can thus make the following assumptions. 92

$$Q_{10} = Q'_{10} = Q \quad (2.9)$$

$$Q_{20} = 1.3Q \quad (2.10)$$

Next, it has been reported[6] that the electronic energy transfer rate from *B* to *A* 93  
state accounts for 0.24 times the total collisional removal from the *B* state. 94

$$\frac{R_{21} + R'_{21} - R_{12}}{Q_{20} + R_{21} + R'_{21} - R_{12}} = 0.24 \quad (2.11)$$

$$\therefore \frac{R_{21} + R'_{21} - R_{12}}{Q} = 0.4105 \quad (2.12)$$

We further know[5, 6] that the collisional transfer from the *B*(0) energy level 95  
populates the nearly degenerate *A*(1) level about four times faster than the *A*(0) 96

level.

97

$$\frac{R_{21} - R_{12}}{R'_{21}} = 4 \quad (2.13)$$

Finally, it was observed[5] that the rate of forward transfer from  $B(0)$  to  $A(1)$  is about 1.6 times the reverse process.

98

99

$$\frac{R_{21}}{R_{12}} = 1.6 \quad (2.14)$$

Collating Equations 2.12–2.14, we obtain a closed set of linear equations. This can be solved to eliminate  $R_{21}$ ,  $R_{12}$  and  $R'_{21}$  in terms of  $Q$  as shown in Equation 2.15.

100

101

$$\begin{bmatrix} R_{21} \\ R'_{21} \\ R_{12} \end{bmatrix} = \begin{bmatrix} 5.1966 \\ 0.4872 \\ 3.2479 \end{bmatrix} Q \quad (2.15)$$

Substituting Equations 2.9, 2.10 and 2.15 into Equations 2.6–2.7 leads to simplified expressions for the populations of the upper electronic states purely as a function of the respective Einstein coefficients and the collisional quenching rate. These are presented in the following Equations 2.16–2.18.

102

103

104

105

$$n_1 = \frac{5.1966Q}{(A_{10} + 4.2479Q)(A_{20} + 6.9838Q) - 16.8780Q} W_{02} n_0 \quad (2.16)$$

$$n'_1 = \frac{0.4872Q(A_{10} + 4.2479Q)}{(A'_{10} + Q)((A_{10} + 4.2479Q)(A_{20} + 6.9838Q) - 16.8780Q)} W_{02} n_0 \quad (2.17)$$

$$n_2 = \frac{(A_{10} + 4.2479Q)}{(A_{10} + 4.2479Q)(A_{20} + 6.9838Q) - 16.8780Q} W_{02} n_0 \quad (2.18)$$

The quenching rate,  $Q$  of excited CH radicals is calculated by using the quenching cross-sections of various species. The quenching cross-sections are measures of the effectiveness of each collision between a given species and an excited CH radical. The

106

107

108

effectiveness of the collision also depends on the velocity of collision between the two species,  $g_j$  and the abundance of the species,  $n_j$ . This relationship is formalized in Equation 2.19.

$$Q = \sum_j g_j \sigma_j n_j$$

$$Q = \sum_j \sqrt{\frac{8kT}{\pi\mu_j}} \sigma_j \frac{pN_A}{RT} X_j \quad (2.19)$$

In Equation 2.19,  $\mu_j$  represents the reduced mass of the colliding CH- $j$  molecules,  $p$  is the pressure,  $N_A$  is Avogadro's Number,  $R$  is the Universal Gas Constant,  $T$  is the temperature, and  $X_j$  is the mole fraction of species  $j$ . The mole fractions of the various species in the flame, as well as the temperature across the flame are obtained from Chemkin simulations. The expression for the reduced mass is given in Equation 2.20.

$$\mu_j = \frac{m_j m_{CH}}{m_j + m_{CH}} \quad (2.20)$$

The quenching cross-sections of various species are obtained from various published papers[7, 8, 9] and are functions of temperature. The functional forms used in this study are presented in Table 2.2.

The term  $W_{02}n_0$  in Equations 2.16–2.18 represents the rate of pumping of the ground state CH radicals. The current excitation scheme targets multiple transitions in the R-bandhead. The pumping rate for each transition is the product of the number of CH radicals present in the appropriate level, the Einstein absorption coefficient for that energy level,  $B_i$  and the amount of laser energy available at the appropriate frequency,  $E_i$ . As a result, the term is actually a summation over the individual energy levels. Equation 2.21 presents this symbolically.

Table 2.2: *The functional form of the quenching cross-sections of various species with CH are provided.*

Species	$\sigma, \text{\AA}^2$
H <sub>2</sub>	$6.1 \exp(-686/T)$
H	$221T^{-0.5} \exp(-686/T)$
O <sub>2</sub>	$8.61 \times 10^{-6} T^{1.64} \exp(867/T)$
OH	$221T^{-0.5} \exp(-686/T)$
H <sub>2</sub> O	9.6
CH <sub>4</sub>	$52.8T^{-0.5} \exp(-84/T)$
CO	8.31
CO <sub>2</sub>	$8.67 \times 10^{-13} T^{3.8} \exp(854/T)$
C <sub>2</sub> H <sub>6</sub>	13.4
N <sub>2</sub>	$1.53 \times 10^{-4} T^{1.23} \exp(-522.1/T)$
C <sub>3</sub> H <sub>8</sub>	22

$$\begin{aligned}
 W_{02}n_0 &= \sum_i B_i I_i n_i \\
 W_{02}n_0 &= \sum_i B_i \frac{E_i}{A_c} \frac{pN_A X_{CH}}{RT} f_i
 \end{aligned} \tag{2.21}$$

Table 2.3 presents the values of  $B_i$  for the transitions targeted by the current  
excitation scheme.[10] Assuming a Gaussian line shape for the laser, and using the line  
strengths from LIFBASE, the relative amount of energy absorbed by each transition  
can be calculated. These values are also presented in Table 2.3.

In Equation 2.21,  $A_c$  is the area of cross-section of the laser beam and  $f_i$  is the  
Boltzmann fraction of the population at the energy level  $i$ . The expression for the  
Boltzmann fraction at the energy level corresponding to the vibrational quantum  
number  $v$  and rotational quantum number  $J$  is given in Equation 2.22.

$$f(v, J) = \frac{\exp\left(\frac{-hcE_v(v)}{kT}\right)(2J+1)\exp\left(\frac{-hcE_r(v, J)}{kT}\right)}{Q_{rv}} \tag{2.22}$$



Table 2.3: *The coefficients of absorption for selected transitions in the CH X( $v = 0$ ) system are provided.*

$N''$	$\lambda$ , nm	$B$ , $\text{m}^2\text{J}^{-1}\text{s}^{-1}$	$E$ (normalized)
R1			
5	387.2698	$7.677 \times 10^9$	0.0568
6	387.1899	$7.665 \times 10^9$	0.1706
7	387.1677	$7.610 \times 10^9$	0.1483
8	387.206	$7.519 \times 10^9$	0.1479
9	387.308	$7.397 \times 10^9$	0.0126
R2			
5	387.2289	$7.539 \times 10^9$	0.1080
6	387.1549	$7.569 \times 10^9$	0.1128
7	387.1371	$7.539 \times 10^9$	0.0841
8	387.1786	$7.464 \times 10^9$	0.1311
9	387.283	$7.354 \times 10^9$	0.0279

The vibrational energy,  $E_v(v)$  of a level is calculated according to Equation 2.23, 136  
while the rotational energy,  $E_r(v, J)$  is calculated according to Equation 2.24. 137

$$E_v(v) = \omega_e \left(v + \frac{1}{2}\right) - \omega_e x_e \left(v + \frac{1}{2}\right)^2 + \omega_e y_e \left(v + \frac{1}{2}\right)^3 - \omega_e z_e \left(v + \frac{1}{2}\right)^4 \quad (2.23)$$

$$E_r(v, J) = \left\{ B_e - \alpha_e \left(v + \frac{1}{2}\right) \right\} J(J+1) - \left\{ D_e + \beta_e \left(v + \frac{1}{2}\right) \right\} J^2(J+1)^2 \quad (2.24)$$

The spectroscopic constants in Equations 2.23 and 2.24 are found in literature[11] 138  
and are provided here in Table 2.4. 139

The rovibrational partition function,  $Q_{rv}$  is a summation over all available vibra- 140  
tional and rotational levels in the particular electronic state. For the ground state 141  
of the CH molecule, there are five available vibrational quantum numbers,  $v = 0$  to 142  
 $v = 4$ . The CH system falls under Hund's Case b and hence, the appropriate rota- 143  
tional quantum number to use is  $N$ . Each vibrational level has twenty-two possible 144  
values for  $N$  from  $N = 1$  to  $N = 22$ . For each rotational quantum number  $N$ , there 145  
are two possible values of  $J$  given by  $N \pm \frac{1}{2}$ . 146

Table 2.4: *Spectroscopic constants for the CH  $X^2\Pi$  level are presented.*

Constant	Value, $\text{cm}^{-1}$
$\omega_e$	2860.7508
$\omega_e x_e$	64.4387
$\omega_e y_e$	0.36345
$\omega_e z_e$	$-1.5378 \times 10^{-2}$
$B_e$	14.459883
$\alpha_e$	0.536541
$D_e$	$1.47436 \times 10^{-3}$
$\beta_e$	$-2.530 \times 10^{-5}$

## CHAPTER 3

147

### EXPERIMENTAL METHODS AND CONSIDERATIONS

148

The current chapter describes the facilities and apparatus used to study the flame characteristics in a Low Swirl Burner. The selection and implementation of diagnostic techniques used in this study are explained, as are data analysis methods used to process the acquired data.

149

150

151

152

#### 3.1 LSB configurations

153

Two configurations of the Low Swirl Burner were tested for this study. There are referred to in what follows as Configurations A and B. Each configuration consists of the reactant flow inlet, the swirler device, the conduit to the combustion zone and the combustion zone itself. All swirlers tested for this work have an outer diameter,  $d_s$  of 38 mm (1.5 in). Other key dimensions of the swirlers tested are presented in Table 3.1.

154

155

156

157

158

159

Each configuration is housed in a high pressure testing facility. The testing facility consists of an air and fuel supply system, a pressure vessel with adequate optical access and an exhaust system for the products. Each testing facility is instrumented to measure temperatures and pressures which are then used to calculate various flow parameters of interest.

160

161

162

163

164

The design of the configurations tested, along with that of their respective test facilities are discussed in greater detail in this section.

165

166

##### 3.1.1 Configuration A

167

Preliminary experiments involving velocity field mapping and flame imaging were performed using this configuration. The schematic of the high pressure test facility

168

169

Table 3.1: *The dimensions of the swirlers used and the respective perforated plates are presented. Each swirler is referred to by its vane angle (as in “ $S_{37^\circ}$ ”).*

Geometric parameter	Swirlers		
	Configuration A $S_{37^\circ}$	$S_{45^\circ}$	Configuration B $S_{40^\circ}$
<b>Swirler data</b>			
Outer diameter, $d_s$ , mm	38	38	38
Diameter ratio, $\frac{d_i}{d_s}$	0.66	0.66	0.66
Vane angle, $\alpha$	$37^\circ$	$45^\circ$	$40^\circ$
Theoretical Swirl Number, $S$	0.48	0.64	variable
<b>Perforated plate data</b>			N/A
Open area, mm <sup>2</sup>	155.97	156.98	-
Blockage, %	71.54	71.36	-
Plate thickness, mm	1.27	1.27	-
Hole pattern	1 - 8 - 16	1 - 8 - 16	-
Hole location (dia), mm	0 - 10.2 - 19.1	0 - 10.2 - 19.1	-
Hole diameter, mm	2.79 - 2.79 - 2.84	2.82 - 2.82 - 2.83	-

housing this configuration is shown in Figure 3.1, while the configuration itself is shown in greater detail in Figure 3.2.

#### 3.1.1.1 Test Facility

Pressurized air is supplied from external tanks and heated in an indirect, gas-fired heat exchanger to about 500 K. The flowrate of the air is metered using a sub-critical orifice flow meter with a 38 mm (1.5 in) bore diameter Flow-Lin orifice plate capable of metering a maximum flow rate of 2.2 kg/s (1 lb/s). The orifice flow meter is instrumented with an Omega PX725A-1KGI pressure transmitter calibrated to a reduced pressure range of 0–2.758 MPa (0–400 psi), a shielded K-type thermocouple and an Omega PX771A-025GI differential pressure transmitter, calibrated to a reduced differential pressure range of 0–68.948 kPa (0–10 psid). The fuel (natural gas) is metered using a similar set up as the air line, with a sub-critical orifice flow meter. The fuel orifice plate is a Flow-Lin orifice plate with a bore diameter of 13.46 mm (0.53 in),

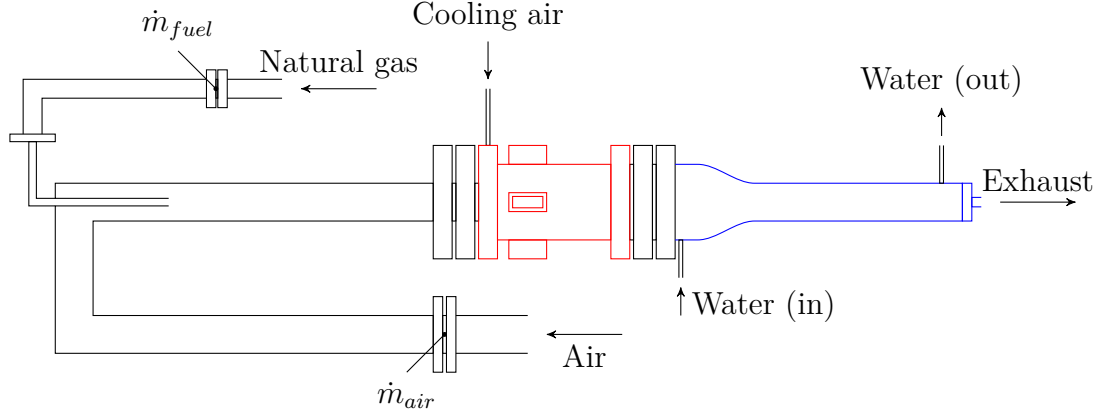


Figure 3.1: A schematic of the high pressure testing facility where Configuration A was operated is shown. The pressure vessel is outlined in red, while the water-cooled exhaust section is outlined in blue. The locations of the orifice flow meters used to measure the mass flow rates of the preheated air and natural gas fuel are indicated.

capable of metering a maximum flow rate of 0.22 kg/s (0.1 lb/s). The upstream pres- 184  
sure is measured using an Omega PX725A-1KGI pressure transmitter (same as the 185  
air line) and the differential pressure is measured using a PX771A-100WDC differ- 186  
ential pressure transmitter with a pressure range of 0–2.489 kPa (100 in H<sub>2</sub>O). The 187  
temperature of the fuel is assumed to be the same as the nominal room temperature 188  
(300 K). 189

The air enters the inlet nozzle of the LSB through a 1.8 m (6 ft) long, 102 mm (4 190  
in) diameter straight pipe section. The fuel flow is choked prior to mixing with the 191  
flow at the head of the straight pipe section. The straight pipe section allows for the 192  
flow to be fully developed, and fully premixed before the reactants enter the burner. 193  
The combustor pressure and temperature are measured at the head of the inlet nozzle. 194  
The pressure is measured by an Omega PX181B-500G5V pressure transducer with a 195  
pressure range of 0–3.45 MPa (0–500 psi), while the temperature is measured using 196  
a K-type thermocouple. 197

The pressure and temperature measurements are used to calculate the four pri- 198  
mary flow parameters (combustor pressure, preheat temperature, reference velocity 199  
and equivalence ratio) for the LSB in real time. All measurements are monitored and 200

recorded during the course of the experiment by a LabView VI.

The pressure vessel enclosing the combustor is designed to withstand pressures of up to 30 atm and is insulated from the combustor by a ceramic liner. Cooling for the pressure vessel and the quartz tube is provided by a flow of cold air introduced at the head of the pressure vessel. The cold air is drawn from the same external tanks as the main air line, but bypassing the heating system. The cold air flow is not metered, but its upstream pressure is coupled to the main air line so as to ensure a steady flow of cold air into the pressure vessel at all operating conditions. Optical access to the combustor is provided through four 25 mm (1 in) thick, 150 mm (6 in)  $\times$  75 mm (3 in) quartz windows located 90° apart azimuthally. The view ports allow the combustor to be imaged from the dump plane to an axial distance of 150 mm (6 in) downstream.

The exhaust from the combustor is cooled by circulating cold water through a water jacket enclosing each section of the exhaust pipe. The length of the exhaust pipe sections is about 1.8 m (6 ft). The exhaust pipe section terminates in an orifice plug that provides back pressure to the combustion chamber. A different diameter orifice is used for each reference velocity condition tested. The exiting products are finally released to the building exhaust system.

#### 3.1.1.2 Low Swirl Burner

The detail of the LSB configuration is shown in Figure 3.2. The premixed, preheated reactants reach the swirler through a converging nozzle that decreases linearly in diameter from from the inlet diameter of 102 mm (4 in) to the outer diameter of the swirler, 38 mm (1.5 in). At the swirler, the flow splits into two streams—one passing through the central section and another picking up swirl by flowing over the vanes in the annular region. The relative flow split between the two streams is controlled by inducing blockage into the central flow by means of a perforated plate. The swirler leads to a constant area nozzle, and is located one diameter upstream of an abrupt

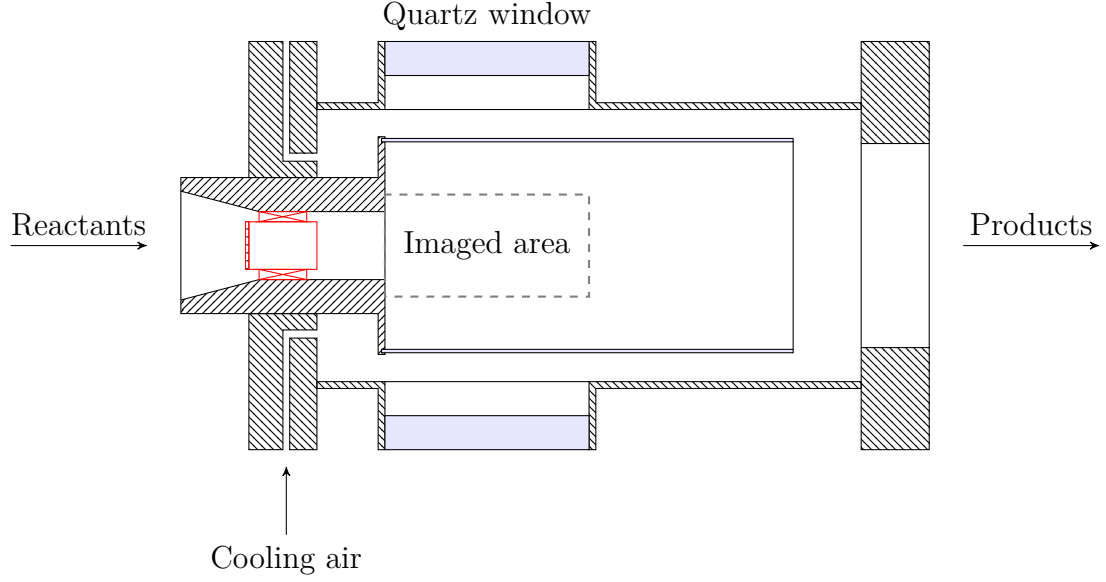


Figure 3.2: A cross-sectional view of Configuration A in the pressure vessel is shown. The reactants enter from the left. The products mix with the cooling air and leave on the right. The location of the swirler in the inlet nozzle is highlighted in red. Also shown is the region of the combustion zone that can be imaged through the quartz windows.

area change. At the area change, the reactants expand from the 38 mm (1.5 in) 228  
diameter nozzle into a 115 mm (4.5 in) diameter combustion zone. This expansion 229  
ratio is chosen so as to avoid confinement effects on the centerline flame flow field.[12] 230

The main combustion zone begins at the dump plane and is enclosed by a GE 231  
quartz tube. The quartz tube is 300 mm (12 in) long and 115 mm (4.5 in) in 232  
diameter. The thickness of the quartz tube is 2.5 mm (0.1 in). 233

### 3.1.2 Configuration B 234

This configuration is used to image the flame structure of the LSB flame using CH 235  
PLIF. A schematic of the flow system of the test facility is shown in Figure 3.3, while 236  
the LSB combustor itself is shown in greater detail in Figure 3.4. 237

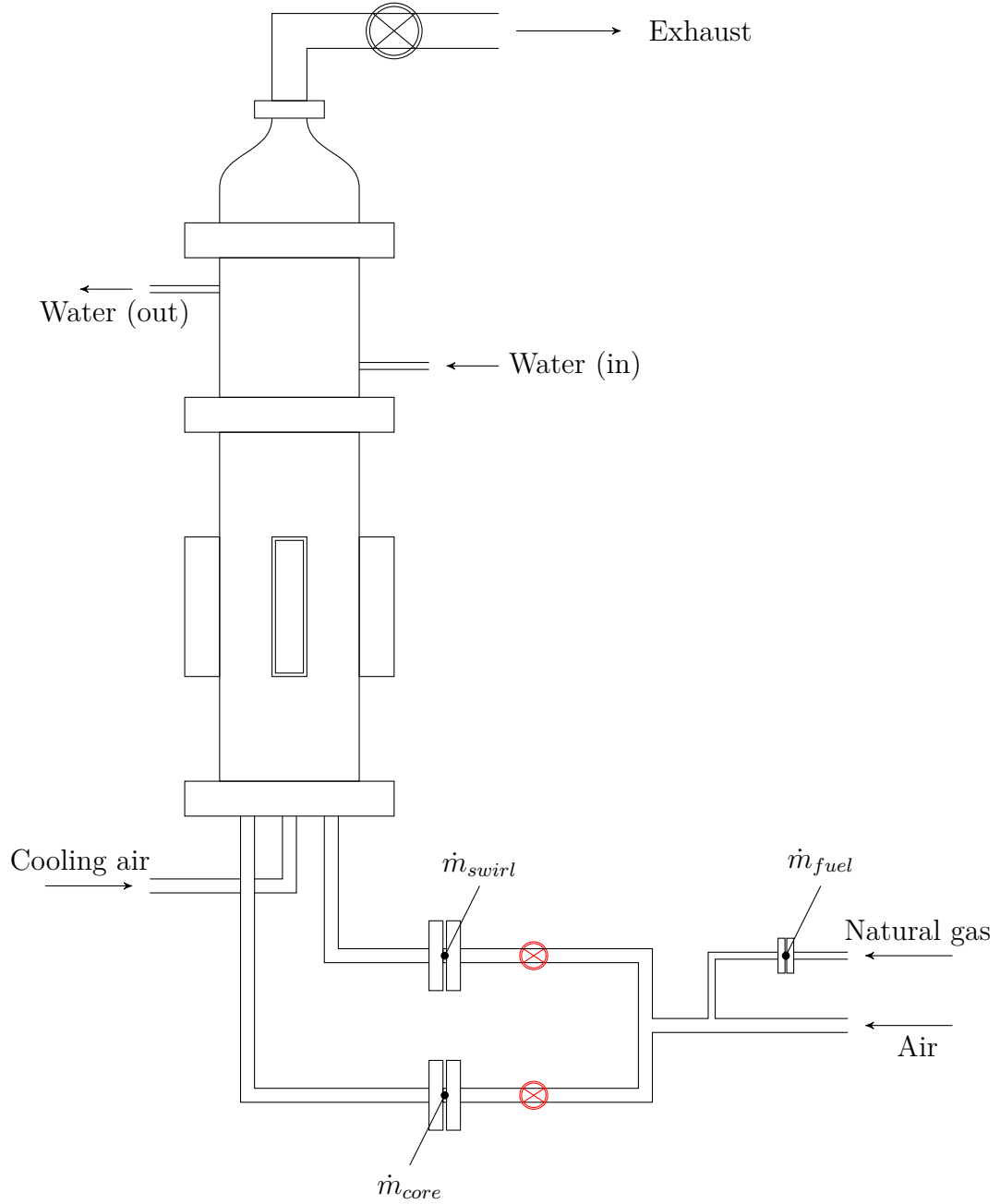


Figure 3.3: A schematic of the high pressure testing facility where Configuration B was operated is shown. The locations of the orifice flow meters on the reactant streams and fuel lines are shown. Valves (shown in red) on the swirl and core flow lines allow for the relative mass flow split to be varied between the two reactant streams. The upstream orifice flow meter on the preheated air line is not shown here.



This test facility shares the upstream supply of preheated air, cold air and fuel (natural gas) with the one used in Configuration A. The flow rate of the preheated air stream is measured using the same orifice flow meter system used in Configuration A—albeit with a smaller 12.921 mm (0.5087 in) diameter bore Flow-Lin orifice plate. The fuel system pressure is regulated from the building supply pressure to a lower required pressure by an adjustable TESCO regulator and metered using a critical orifice flow meter. The critical orifice on the fuel line has a bore diameter of 0.8128 mm (0.032 in). The pressure upstream of the critical orifice is measured using an Omegadyne PX409-1.5KGI pressure transmitter with a range of 0–10.34 MPa (0–1500 psig) and the pressure downstream of the critical orifice is measured using a Dwyer 626 series pressure transmitter with a range of 0–3.45 MPa (0–500 psig). The downstream pressure can be used to verify if the critical orifice is choked during operation. The temperature of the fuel is measured upstream by a K-type thermocouple.

The air system is choked with a 5.41 mm (0.213 in) diameter critical orifice before mixing with the fuel. A short distance after mixing, the reactants are split into two separate streams for the central flow and the swirl flow. The central flow rate is measured using a 9.271 mm (0.365 in) diameter sub-critical orifice, instrumented with a Dwyer 626 series pressure transmitter with a range of 0–4.14 MPa (0–600 psig) for measuring the upstream pressure, a K-type thermocouple for measuring the upstream temperature and an Omega PX771-300WCDI differential pressure transducer with a range of 0–74.65 kPa (0–300 in H<sub>2</sub>O). The swirl flow rate is measured similarly, using a 11.68 mm (0.46 in) diameter sub-critical orifice, a Dwyer 626 series pressure transmitter with a range of 0–5.52 MPa (0–800 psig), a K-type thermocouple and another Omega PX771A-300WCDI with a differential pressure range of 0–74.65 kPa (0–300 in H<sub>2</sub>O). The relative flow split between the two reactant streams is controlled

by partially closing gate valves on the two lines.

The cooling air flow line is choked, but the flow rate is not metered. All measurements are monitored and recorded by a LabView VI.

The pressure vessel is rated for pressures in excess of 30 atm and is insulated from the combustor by a flow of cold air. The cold air enters the pressure vessel through two inlet ports and passes through a layer of steel ball bearings which renders the flow uniform spatially. The central and swirl flow reactant streams enter through separate ports and connect to the combustor. The pressure vessel has four viewports located 90° apart for optical access. Each viewport is covered by a 25 mm (1 in) thick, 178 mm (7 in)  $\times$  50 mm (2 in) quartz window. The LSB exit is located approximately halfway between the top and bottom edges of the window, allowing about 88.9 mm (3.5 in) of the combustion zone to be imaged through the window. Similar to Test Rig A, the exhaust section is cooled by circulating cold water through an enclosing water jacket. An adjustable gate valve on the exhaust line provides the back pressure necessary to pressurize the combustor. The products are vented into the same building exhaust system as Configuration A.

### 3.1.2.2 Low Swirl Burner

The design of this LSB configuration is presented in Figure 3.4. As described earlier, the reactants reach the LSB swirler device through two separate streams. The core/central stream passes through a plenum chamber which is filled with steel ball bearings before approaching the swirler through a smoothly contoured nozzle with a high contraction ratio. The annular/swirl stream reaches the swirler directly through a separate contoured nozzle. The contraction ratio is chosen to inhibit the formation of thick boundary layers in the reactant streams. The core stream passes through the central portion of the swirler, while the annular stream picks up swirl by passing through the vanes of the swirler. The swirler lacks a perforated plate covering the

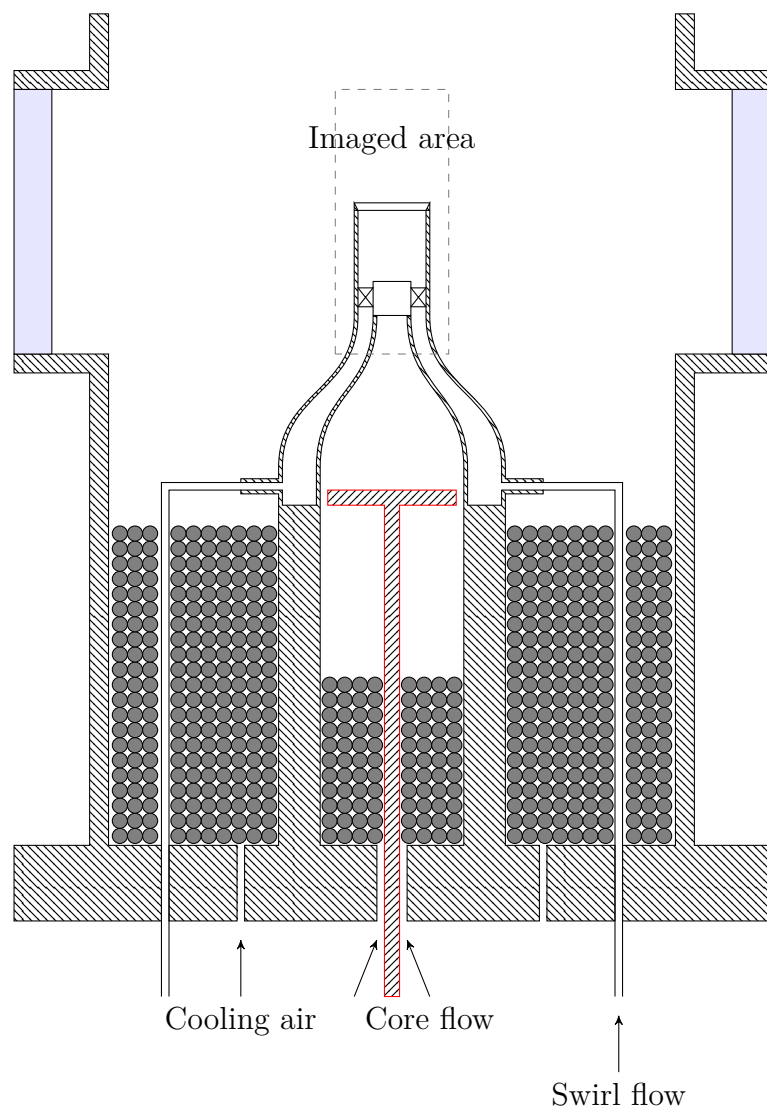


Figure 3.4: A cross-sectional view of Configuration B in the pressure vessel is shown. The reactants enter from below in two separate streams (core flow and swirl flow), along with cooling air. Stainless steel ball bearings inside the plenum chamber and outside make the core flow and the cooling air flow spatially uniform. The turbulence generator is located within the plenum and is outlined in *red*.

central region as the primary function of the plate—regulating the relative mass flow split—is performed by the test facility itself.

The swirler device is located at the beginning of a constant area nozzle which is 57.2 mm (2.25 in) in length. Following this, the reactants expand into the combustion zone.

Unlike in Configuration A, there is no dump plane or quartz tube to provide confinement to the combustion zone. The co-flow of cold air provides insulation to the walls of the pressure vessel. Also, as mentioned earlier, the relative mass flow split between the central and annular flows can be controlled directly. Finally, the level of turbulence in the central flow can be adjusted by use of a turbulence generator[13] located upstream in the plenum chamber.

## 3.2 Diagnostics

### 3.2.1 Laser Doppler Velocimetry

The velocity field of the LSB is mapped using a TSI 3-component LDV system. Three wavelengths (514 nm, 488 nm and 476 nm) are separated from the output of a 5 W Argon ion laser by an FBL-3 multicolor beam generator. The individual beams are split into two coherent beams which are then focused to intersect and produce interference fringes within an ellipsoidal measurement volume with dimensions of the order of 100  $\mu\text{m}$ . For this purpose, two transceiver probes are mounted 90° apart about the axis of the LSB. The setup is illustrated as a schematic in Figure 3.5. One transceiver probe focuses the 514 nm and 488 nm beams in planes perpendicular to each other, while the second probe focuses the 476 nm beams orthogonal to the other two beams. Particles in the flow field crossing the interference fringes scatter the laser light elastically and produce a sinusoidal signal whose frequency is proportional to the velocity of the particle. The transceiver probes collect this scattered light and each wavelength is detected separately by a PDM-1000-3 three-channel photodetector

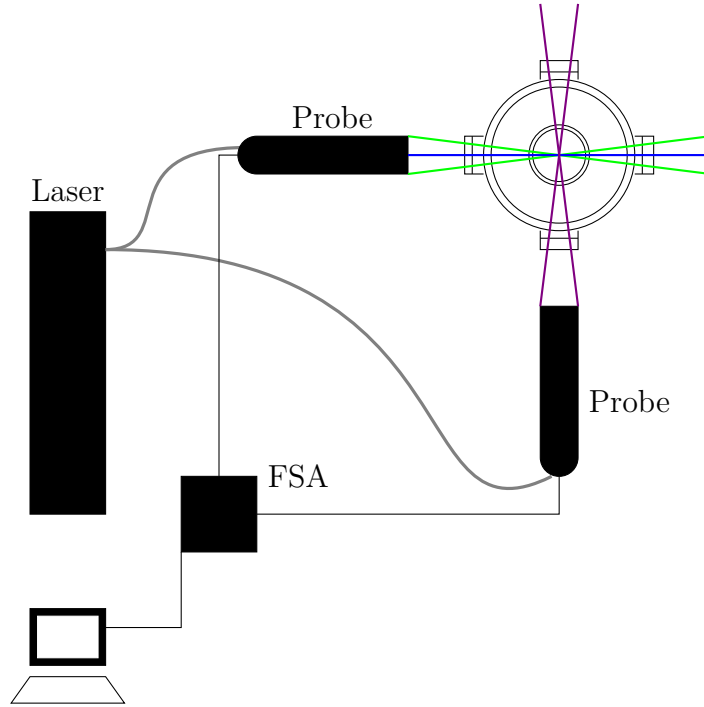


Figure 3.5: The schematic shows the setup employed to map the velocity field of the LSB combustor using Laser Doppler Velocimetry. Three pairs of orthogonal beams are separated from the Argon Ion Laser output and conveyed by fiber optic cables (gray) to optical probes mounted  $90^\circ$  apart about the axis of the LSB combustor. The green, blue, and violet beams in the schematic represent the 514 nm, 488 nm and 476 nm wavelengths. The signal is collected by the transceiver probes and analyzed by the FSA module. The results are saved for further analysis.

module. The output from the photodetector is processed by an FSA-3500-3 signal processor. The resulting three components of the particle/flow velocity are recorded by the FlowSizer software.

Since the concentration of particulate matter (primarily dust particles) in the airflow is very low, the flow needs to be artificially seeded to facilitate LDV measurements in a reasonable amount of time. The choice of seeding particles to be used and their mean diameter are decided by the characteristics of the flow to be imaged.[14] Since the LSB flow field is a reacting one, the particles need to have high melting points. Further, the particles need to be small enough to follow the flow closely and large enough or reflective enough to scatter light efficiently in the measurement volume. Based on these requirements, commercially available alumina particles with a mean particle diameter of  $5\text{ }\mu\text{m}$  were chosen for this study. In order to uniformly seed the flow, a novel seeding generator was designed as described in Appendix A. The seeding particles were introduced slightly upstream of the 1.8 m (6 ft) long straight pipe section in Test Rig A.

LDV data is only acquired at atmospheric pressure conditions. At high pressure conditions, the reacting LSB flow field produces sharp refractive index gradients that rapidly shift in the turbulent flow field. This causes strong beam steering effects making it very difficult for the laser beams to reliably intersect within such a small measurement volume. The long distance traveled by the beams in the test rig further exacerbate this problem, making LDV data nearly impossible to acquire at such conditions.

### 3.2.2 $\text{CH}^*$ chemiluminescence

The LSB flame is imaged using one of two 16-bit intensified CCD cameras—PI Acton 1024 $\times$ 256 or 512 $\times$ 512 pixels—with a 28 mm f/2.8 camera lens.  $\text{CH}^*$  chemiluminescence is filtered using a bandpass filter centered on 430 nm with a FWHM of 10 nm.

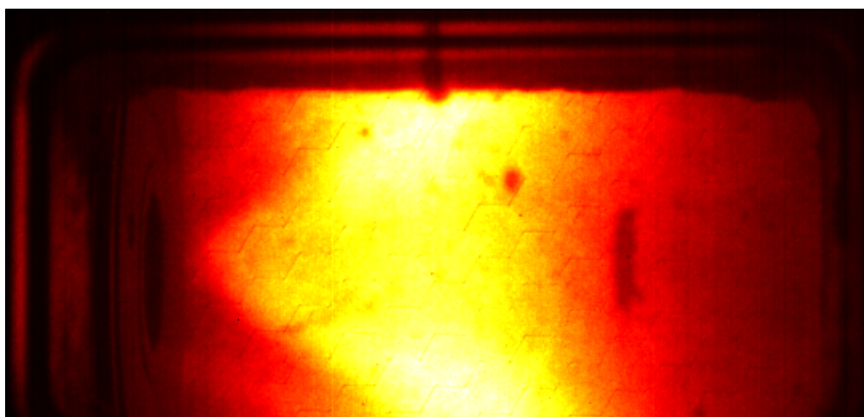
At each operating condition, 100 instantaneous images are acquired with an exposure  
of 1 ms. An additional 100 instantaneous images are acquired with no flame and  
averaged to yield the background for correcting the flame images.

CH\* chemiluminescence has several advantages over flame chemiluminescence  
from other radicals such as OH\*, C<sub>2</sub>\*, etc. First, the CH\* emission occurs around 430  
nm and is less affected by blackbody radiation from the walls of the combustor com-  
pared to longer wavelength detection, e.g., C<sub>2</sub>\*, which emits around 514 nm. Second,  
the intensity of the chemiluminescence from CH\* is known to scale well with heat  
release in the combustor[15], unlike C<sub>2</sub>\*. Third, the emitted light can be gathered  
with high quantum efficiency by the intensified CCD cameras available for this study.  
Particularly, the quantum efficiency of the 18 mm Gen III HB filmless intensifier used  
by the 512×512 camera is about 45% at 430 nm, compared to about 10% at 310 nm,  
where OH\* chemiluminescence peaks.

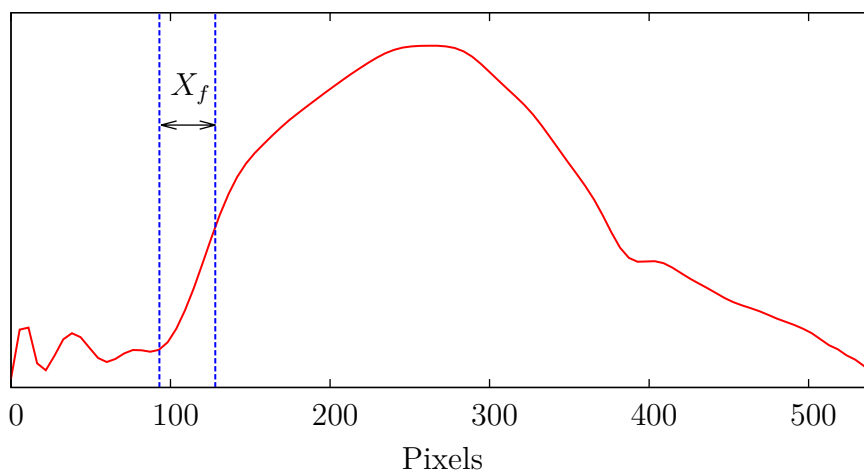
### 3.2.2.1 Image Processing

The flame chemiluminescence images acquired are background-corrected and aver-  
aged. The resulting mean is the line-of-sight integrated, time-averaged image of the  
flame. Strictly speaking, this is not the same as a real average obtained from a long  
exposure image as the instantaneous images are obtained through a periodic sam-  
pling process and hence, are prone to statistical errors. However, the behaviour of  
the flame can be assumed to be sufficiently random that the mean obtained is ad-  
equately representative of the true average. Figure 3.6a shows a typical mean CH\*  
chemiluminescence image prepared in this manner.

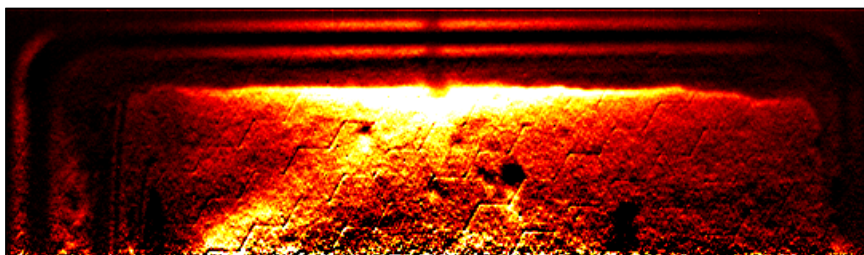
Even when background-corrected, the walls of the combustor are not at zero in-  
tensity in the average chemiluminescence image. This is particularly noticeable near  
the dump plane where there is no flame present and yet the walls are clearly illumi-  
nated. The source of this background illumination is mostly the chemiluminescence



(a) *Average  $CH^*$  chemiluminescence image*



(b) *Centerline  $CH^*$  chemiluminescence intensity*



(c) *Abel deconvoluted half-image*

Figure 3.6: *These images illustrate the processing of a typical  $CH^*$  chemiluminescence dataset. The top image is the mean of 100 frames and shows the LSB flame at 9 atm. The flame standoff distance is calculated by locating the inflection point in the smoothed intensity profile (middle). An Abel deconvolution (bottom) can be used to highlight the flame brush and measure the angle of the flame.*



from the flame scattering off the combustor and pressure vessel walls. The contribu- 371  
tion from blackbody radiation from the heated walls is less significant in the narrow 372  
wavelength range imaged. This is evident from images acquired immediately after a 373  
flame blowout which show the walls to be nearly dark. 374

The averaged chemiluminescence image allows us to measure the flame stand- 375  
off distance by following the intensity profile along the centerline of the combustor. 376  
The intensity profile rises sharply when passing the flame standoff location. Thus, 377  
the flame standoff location can be ascertained by finding the inflection point in the 378  
intensity profile. 379

The profile of the average chemiluminescence intensity along the centerline of the 380  
sample case from Figure 3.6a is shown in Figure 3.6b, showing the flame standoff 381  
distance. The distance from the dump plane, measured in number of pixels on the 382  
image and scaled by the appropriate magnification factor yields the flame standoff 383  
distance,  $X_f$ . The determination of the flame standoff location by this method pro- 384  
vides a suitable and deterministic means to locating the leading edge of the flame 385  
front. 386

The average image can be processed further to yield more spatially resolved in- 387  
formation about the flame brush. Under the reasonable assumption that the average 388  
LSB flame is axially symmetric about the centerline of the combustor, a tomographic 389  
deconvolution technique called an Abel deconvolution[16] can be used to convert the 390  
line-of-sight integrated image to a radial map of chemiluminescence intensity. In 391  
effect, this shows the shape and structure of the average flame brush. The Abel 392  
deconvolution of the sample data from Figure 3.6a is shown in Figure 3.6c. 393

The Abel-deconvoluted image provides an relatively easy means to determining 394  
the angle of the flame brush. A straight line joining two points located at the center 395  
of the flame brush intersects the axis of the combustor at this angle. The angle of 396  
the flame is denoted by  $\theta_f$ . 397

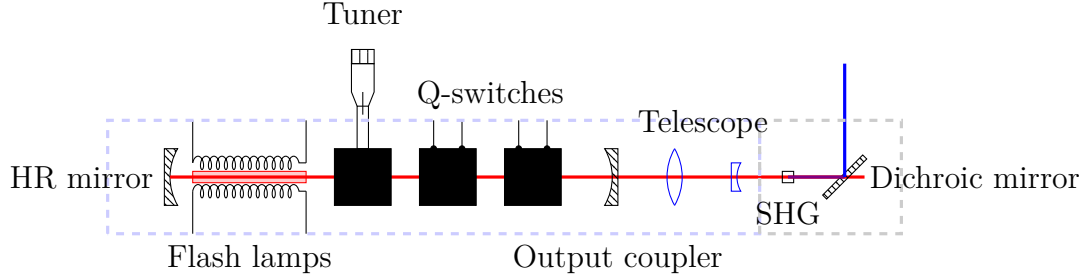


Figure 3.7: A schematic of the components of the PAL 101 Alexandrite laser is shown. The resonator formed by a High Reflection (HR) mirror and an output coupler is built around an alexandrite rod (*red*) pumped by flashlamps. The frequency of the output is selected by a tuner mechanism. Only one of the two Q-switches was used for this study. The laser beam is reduced in diameter by a collimating telescope (*blue*) before passing through the Second Harmonic Generator (SHG). The UV beam is separated from the fundamental by a dichroic mirror and exits the laser. The fundamental beam terminates within the laser in a beam dump.

Using the Abel deconvolution to study the flame brush suffers from two main drawbacks. First, the system of equations describing the Abel deconvolution is only valid as long as the entirety of the flame is visible. This is only satisfied in the initial region of the LSB where the diameter of the flame brush is smaller than the height of the optical viewport. At further downstream locations, the flame is not imaged in its entirety. This causes the spurious bright regions near the top of the window in Figure 3.6c. The second limitation of the Abel deconvolution technique stems from the high incidence of errors along the centerline (where  $r \rightarrow 0$ ). Due to this, any study of the flame brush thickness at the flame stabilization point—a metric of considerable importance—is all but impossible using this tomographic technique.

### 3.2.3 CH Planar Laser-Induced Fluorescence

The CH PLIF setup uses the frequency-doubled output of a Light Age PAL 101 alexandrite laser tuned to  $\lambda \approx 387.2$  nm. The design of the laser is shown schematically in Figure 3.7. The active medium is a 150 mm (6 in) long, 5 mm (0.197 in) diameter alexandrite rod. The rod is placed between two flashlamps within the resonator cavity formed by two spherical mirrors. A birefringent tuning mechanism

is placed within the resonator to allow the user to select the frequency of the out- 414  
put beam. The tuning mechanism is coupled to a micrometer whose reading relates 415  
linearly to the output wavelength. The tuning mechanism allows the fundamental 416  
wavelength to be varied between 720–780 nm, with peak gain at about 755 nm. The 417  
resonator cavity also contains two Q-switches, which allow the laser to optionally 418  
operate in double-pulsed mode. For this study, however, only one Q-switch is used 419  
and the laser is operated in single-pulsed mode only. 420

The diameter of the fundamental beam exiting the output coupler is reduced by a 421  
collimating telescope. This is done in order to increase the efficiency of conversion of 422  
the frequency-doubling crystal. The second harmonic portion of the beam is separated 423  
from the fundamental by a dichroic mirror and exits the laser. The fundamental beam 424  
is terminated at a beam dump within the laser. The exit beam diameter is about 1 425  
mm. 426

The alexandrite laser is capable of operating at frequencies of up to 15 Hz. Laser 427  
power is controlled primarily by varying the voltage applied to the flash lamps. When 428  
operating with a high flash lamp voltage, it is recommended that the frequency of 429  
pulsing be reduced to allow more time to dissipate the heat build up within the 430  
alexandrite rod. All experiments conducted as part of this study operated the laser 431  
at 10.0 Hz. 432

The typical power output of the laser is about 15 mJ/pulse. The pulsewidth of 433  
the laser is about 60-80 ns and is observed to decrease with increasing flash lamp 434  
voltage. The linewidth of the fundamental beam is determined by the manufacturer 435  
to be 150 GHz at  $\lambda = 775$  nm. Assuming the spectral profile of the laser to be a 436  
Gaussian, the linewidth of the frequency-doubled beam can be determined. The Full 437  
Width at Half Max (FWHM) of a Gaussian curve scales linearly with the standard 438  
deviation of the curve. When convoluted with itself, the new standard deviation is 439  
 $\sqrt{\sigma^2 + \sigma^2}$  or  $\sqrt{2}$  times that of the original curve. Thus, the new linewidth is  $150 \times \sqrt{2}$  440

= 212 GHz or  $7.07 \text{ cm}^{-1}$ . In wavelengths, this represents a spread of about  $1.06 \text{ \AA}$ . 441

### 3.2.3.1 Imaging system 442 443

All LIF imaging is performed with an intensified PI Acton  $512 \times 512$  camera. The 444  
intensified camera is equipped with an 18 mm Gen III HB filmless intensifier with 445  
a quantum efficiency of about 45% in the 420–440 nm range. The lens is chosen 446  
depending on imaging requirements of each experiment. In all cases, elastic scattering 447  
from the laser beam is attenuated by a 3 mm thick GG 420 Schott Glass filter. 448

### 3.2.3.2 Laminar Flame setup 449 450

Preliminary experiments to evaluate the CH PLIF technique are performed on a 451  
laminar flame. The choice of a laminar flame as the subject allows us to neglect 452  
effects of strain and turbulence on the flame. Further, laminar flames are more readily 453  
simulated by reaction kinetics packages like Chemkin with high fidelity. 454

These experiments are conducted on an laminar, methane-air flame stabilized on 455  
an unpiloted Bunsen burner with an inner diameter of 10.16 mm (0.4 in). The air 456  
flow rate is measured and regulated using a Dwyer rotameter with a range of 0–20 457  
SCFH calibrated using a Ritter drum-type gas meter. The natural gas flow rate is 458  
metered using a Matheson FM 1050 602 rotameter with a range from 0–1230 SCCM. 459  
This flowmeter is calibrated using a Sensidyne Gilibrator 2 bubble flow meter system. 460

### 3.2.3.3 Laser Wavelength Calibration 461 462

As described earlier, the output wavelength of the PAL 101 alexandrite laser is 463  
controlled using a micrometer-coupled birefringent tuning mechanism. The wave- 464  
length of the laser beam varies linearly with the micrometer reading. Initially, the 465  
manufacturer-supplied calibration for the micrometer was found to be inaccurate. 466

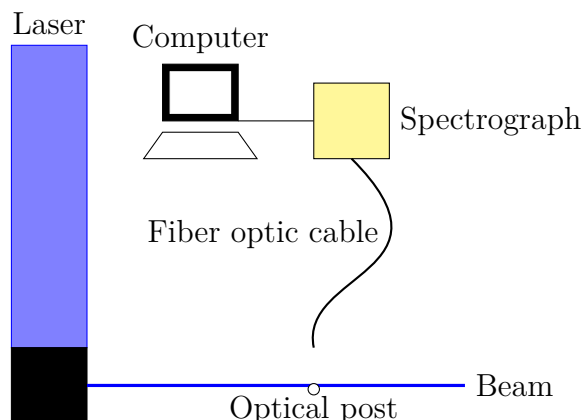


Figure 3.8: The figure above shows the schematic of the experiment performed to calibrate the wavelength of the laser output. The laser output (containing mostly UV, but also a small portion of the fundamental frequency) is glanced off a steel optical post. The scattered light is gathered by a fiber optic cable and sent to a spectrometer. The spectrum is analyzed to track the location of the fundamental frequency with tuner position. The UV peak is not tracked as the spectrometer is not calibrated for that wavelength.

This required an experiment to calibrate the laser output wavelength against the mi- 467  
crometer reading in order to determine the slope and offset of the calibration curve 468  
accurately. 469

A schematic of this experiment is shown in Figure 3.8. The laser beam is glanced 470  
off a steel optical post and the scattered light is collected using a fiber-optic cable cou- 471  
pled to an Ocean Optics HR 2000 spectrometer. The spectrometer is pre-calibrated 472  
using 50 wavelengths in the 400–850 nm range from the output of a Neon discharge 473  
lamp source. The spectrometer is also intensity corrected over this range using a 474  
black body source. The estimated error in the resolution of the device is about 0.1 475  
nm (1 Å). 476

The laser micrometer is traversed from 0.600 in to 0.625 in in steps of 0.001 in. 477  
The experiment is repeated by traversing the micrometer from 0.625 in back to 0.600 478  
in along the same points to ensure repeatability and estimate the variation due to 479  
hysteresis. The calibration is performed using at the fundamental wavelength of the 480  
laser as the second harmonic wavelength falls outside the spectrometer’s range. Each 481  
spectrum recorded is integrated over 512 ms and averaged over 10 such acquisitions. 482

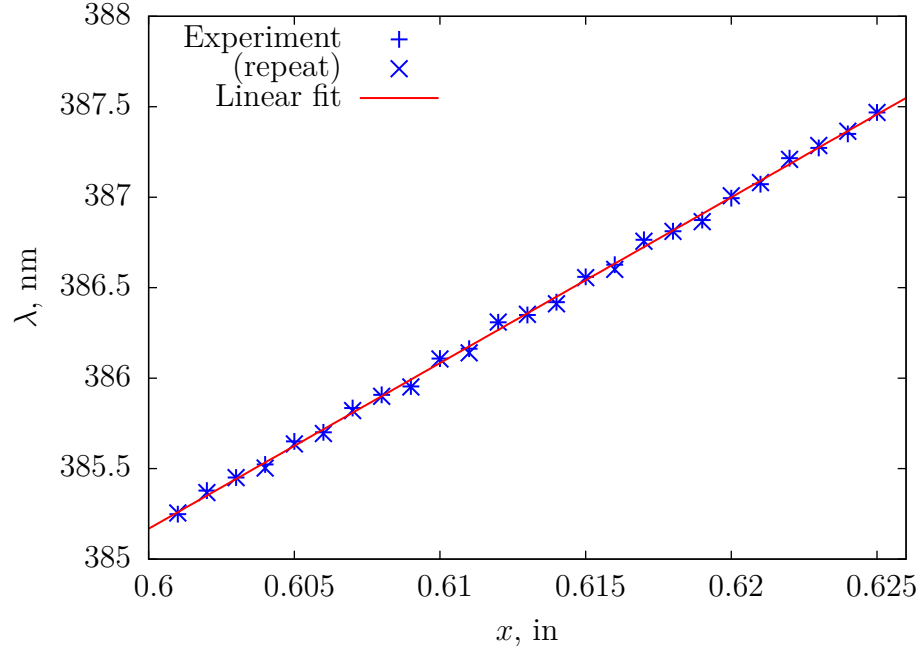


Figure 3.9: The wavelength of the second harmonic beam of the laser is plotted above against the tuner position( $x$ ). The data shows excellent repeatability and falls on a linear trend. The equation for the linear curve fit is  $\lambda = 330.213 + 91.5908x$ , where the units of  $\lambda$  and  $x$  are nm and in, respectively.

The background-corrected peak of the spectrum is then modeled as a Gaussian and the location of the center of the Gaussian waveform is recorded.

The results from this experiment are shown in Figure 3.9. The plot demonstrates that the variation of the second harmonic wavelength (obtained by halving the fundamental wavelength) with the position of the tuner micrometer is linear. Further, there is little difference between the measurements taken while increasing and decreasing the micrometer position. This indicates that any effects of hysteresis in the micrometer position are minimal. The calibration equation relating the micrometer position to the output wavelength is obtained by applying a linear curve fit to the data points on the graph as shown in Figure 3.9.

## CHAPTER 4

493

### CH PLIF SIGNAL MODELING AND VALIDATION

494

#### 4.1 CH PLIF Development/Preliminary Experiments

495

The CH PLIF imaging system was evaluated for use in imaging hydrocarbon flames by performing two preliminary experiments. First, an excitation scan was performed to locate the optimal wavelength to excite the CH radicals in a typical hydrocarbon flame. The variation in this optimal wavelength with temperature and pressure was calculated and found to be within acceptable bounds. Second, a test of the linearity of the LIF signal with respect to the incident laser intensity was performed. The setup and results of these experiments are described in the following subsections.

##### 4.1.1 Excitation scan

503

An excitation scan is performed by tuning the output of the alexandrite laser from  $\lambda = 387.077$  nm to 387.260 nm. This serves two purposes. First, it locates the optimal wavelength to excite the CH radicals that results in the highest fluorescence yield. Second, the variation of the signal intensity can be compared with simulated profiles from LIFBASE or other spectroscopic calculations and our estimation of the laser linewidth can be validated. Knowing the laser linewidth accurately is important for modeling the LIF signal. This aspect will be discussed in further detail later in this thesis/chapter FIXME.

A schematic of the excitation scan experiment is shown in Figure FIXME. The intensified PI Acton 512×512 camera described in Section 3.2.2 is used to image a premixed, laminar methane-air flame operating at close to stoichiometric conditions. The laminar flame is stabilized on the Bunsen burner described in Section 3.2.3.2. The

alexandrite laser is operated at a power of 16 mJ/pulse in the second harmonic. The sheet forming optics consist of a +50 mm cylindrical lens and a +250 mm spherical lens placed 300 mm apart. The optics form the beam into a collimated sheet about 25 mm (1 in) tall, focused to a thickness on the order of 100  $\mu\text{m}$  at the flame location. The sheet passes through the center of the flame and the edges of the sheet are blocked by razor blades to prevent reflections from the burner from saturating the camera.

The induced fluorescence in the flame sheet is imaged perpendicularly by the intensified camera using an 85 mm f/1.8 Nikon AF Nikkor lens. This gives a magnification of approximately 62  $\mu\text{m}/\text{pixel}$ . The camera is triggered by the flash lamp sync signal from the laser system and the intensifier is gated over 300 ns, encompassing the 70 ns laser pulse. The long gate width gives the intensifier enough time to prepare to receive the fluorescence, preventing signal loss due to iris-ing. The gate width is still short enough that minimal flame chemiluminescence or ambient lighting is recorded in the images. 100 instantaneous images are acquired for each excitation wavelength to acquire a good estimate of the mean fluorescence signal,  $\mu_{sig}$ .

Figure FIXME shows a sample CH PLIF image from this dataset. The images are background-corrected by subtracting the laser scattering (recorded without the flame). The fluorescence signal is calculated from these images using three alternate approaches.

In Method I, two “windows” are identified that include the straight sections of the laminar flame. The average fluorescence signal in each frame is calculated by taking the average of all the emitting pixels in the two windows. A pixel is designated as an emitting pixel if its intensity exceeds the standard deviation of a typical background pixel by at least a factor of five. The average of this value over all the frames is designated as the mean fluorescence signal,  $\mu_{sig}$ . In Method II, the intensity of the pixels is integrated over a straight line connecting the inner and outer edges of the flame. The straight line is chosen along the beam so that the beam intensity does



not vary along the integration path. The integration is performed on the left and right arms of the flame, giving two readings per frame. The mean of these values over all the frames is recorded as the mean fluorescence signal,  $\mu_{sig}$ . In Method III, the midpoints of the straight lines from Method II are located and the average of their intensities, over all the frames is recorded as the mean fluorescence signal,  $\mu_{sig}$ . The regions of interest for each of these methods is highlighted in Figure FIXME.

The result of this investigation is shown in Figure FIXME. The calculated mean fluorescence signals from the three methods are plotted against a LIFBASE simulation of the absorption spectrum of the CH  $B-X$  transition. The profiles are appropriately scaled to match the LIFBASE simulation at the maximum value and at the minimum value. The LIFBASE simulation is performed for a thermalized system at 1800 K, at atmospheric pressure. Further, the instrument linewidth is specified to be the same as our estimate of the laser linewidth (1.06 Å).

The profiles of the calculated and scaled mean fluorescence signals are observed to agree extremely well with the LIFBASE simulation result. The discrepancies between the three methods is minimal.

The results indicate that the optimal excitation wavelength, corresponding to the highest mean fluorescence signal, is about 387.2 nm. For the rest of the experiments performed in this work, the laser is operated at this wavelength. The results also help verify that the calibration of the micrometer is accurate and the wavelengths are precisely adjustable. Finally, the results validate that our estimated laser linewidth, 1.06 Å, is accurate. This value can now be used in subsequent calculations of the LIF signal levels.

#### 4.1.2 Linearity test

As explained in Chapter FIXME, the variation of the fluorescence signal with the excitation laser intensity exhibits a saturation curve. In the weak excitation limit,

the variation is linear and scales with the energy input. For reasons explained in Chapter FIXME, it is preferred to operate in this linear regime.

An experiment is performed to verify the linearity of the system response at the intensities at which the flames are imaged for this work. The schematic of the setup is shown in Figure FIXME. The laser is tuned to the optimal wavelength as determined in Section 4.1.1, and operated at 10 Hz. The frequency-doubled beam is directed at a steady, laminar, methane-air Bunsen flame operating at a slightly rich stoichiometry. The edges of the beam are clipped by an aperture to produce a sharp edge and to avoid unnecessary reflections from the burner. No optics are used to refract the beam in any way.

The flame is imaged by the PI Acton 512×512 intensified camera equipped with a 50 mm, f/1.8 AF Nikkor lens. Elastic scattering is attenuated by a 3 mm thick GG 420 Schott glass filter. The magnification achieved by this set up is about 44  $\mu\text{m}/\text{pixel}$ . The LIF signal from the flame is recorded in 300 ns gates and accumulated 150 times before being read out. For each case, a corresponding laser scattering image is also recorded for estimating the background. The flame chemiluminescence and ambient background are also recorded for the same purpose.

For this experiment, varying the intensity of the laser beam by changing the flash lamp voltage or even the Q-switch timing is not preferred as either would alter the pulse width of the beam. Instead, quartz disks and blocks of varying thickness are introduced into the beam to produce an intensity loss, while preserving all other characteristics of the beam. The quartz elements decrease the intensity of the laser beam through reflection, scattering and absorption. The stray reflections and scattering from the quartz elements are contained by enclosing the elements in a box and preventing these from being recorded by the camera. In this manner, the laser power is varied from 10 mJ/pulse to 0.5 mJ/pulse and back.

The acquired images are background-corrected and the intensity is conditionally

averaged over pixels with a non-zero intensity in the region where the fluorescence occurs. The average fluorescence intensity values thus obtained are plotted against the corresponding laser intensity and shown in Figure FIXME. A sample image highlighting the region of interest is also shown alongside.

The LIF signal is observed to increase monotonically with increasing laser intensity. At the lower intensities, the variation is very nearly linear, with marginal scatter and only one significant outlier. At intensities above  $1 \text{ J/cm}^2$  however, there is significant scatter in the data and the linear trend obtained from the low intensity cases cannot be reliably extended over this region.

The results indicate that as long as the intensity of the laser sheet is kept below  $1 \text{ J/cm}^2$ , the assumption of operating in the linear regime is valid.

## 4.2 Fluorescence Signal Modeling

In Chapter FIXME 2, we derived the expression for the LIF signal as a function of the thermodynamic conditions and the local composition. The expression requires the pre-knowledge(?) of several spectroscopic constants of the CH system.

As described in Chapter FIXME 2, the excitation scheme used in this study produces fluorescence through a three-step process. First, the CH radicals in the ground state  $X^2\Pi, v = 0$  are excited by the incident radiation to the second electronically excited state  $B^2\Sigma^-, v = 0$ . This excitation occurs near the R-bandhead and targets the ground state CH radicals present in the rotational energy levels,  $N = 5$  through 9. The upper electronic state  $B^2\Sigma^-, v = 0$  is nearly degenerate with the  $A^2\Delta, v = 1$  energy level. This leads to the population of the  $A^2\Delta, v = 0, 1$  energy levels due to collisional energy transfer. The resulting fluorescence collected is primarily the result of three spontaneous transitions —  $A \rightarrow X(1, 1)$ ,  $A \rightarrow X(0, 0)$  and  $B \rightarrow X(0, 1)$ . These transitions are shown in Figure FIXME.

The primary goal of this exercise of modeling the CH fluorescence signal intensity

is to gage the feasibility of using CH PLIF to study various premixed flames, rather  
than to quantitatively calculate the amount of CH present in the flames. As such,  
we are more interested in the order of magnitude of the PLIF signal, rather than the  
absolute value of it.

The intensity of the CH fluorescence signal may be written as a function of the  
amount of CH radicals present in the excited state and the probability of spontaneous  
emission from said state. Symbolically, this may be written as shown in Equation  
4.1.

$$S = nVA \quad (4.1)$$

In Equation 4.1,  $S$  is the total number of photons emitted per unit time,  $n$  is the  
number of excited CH radicals in a unit volume,  $V$  is the volume from which the  
signal is observed. The Einstein coefficient for spontaneous emission,  $A$  represents  
the probability of spontaneous emission between the two involved energy states. The  
predicted signal intensity represents the total number of photons emitted in all di-  
rections. In reality, only a fraction of these emitted photons will be recorded by the  
collection system. This fraction is a function of the experimental setup and depends  
on the collection angle, the efficiency of the optics and the detector used to record the  
signal. This fraction is left out because our objective is only to predict the relative  
variation in the signal between various premixed flames.

This formulation of the signal intensity implicitly makes the following assumptions.

1. The fluorescence emission is predicted at steady state.
2. The collection volume is optically thin and an emitted photon is not reabsorbed  
within the flame itself. This is a reasonable assumption to make, since the flame  
thickness and the thickness of the laser sheet are both typically quite small.

As described earlier, an accurate model of the CH system should involve five energy

levels —  $X(0)$ ,  $B(0)$ ,  $A(1)$ ,  $A(0)$ , and  $X(1)$ <sup>1</sup>. Such a model would also have to ac- 646  
count for collisional transfers between each of these levels, in addition to spontaneous 647  
and stimulated transitions. The mathematical solution quickly becomes complicated 648  
and tedious. Further, it would involve several rate coefficients that have not been 649  
measured in experiments done so far. 650

### 4.3 Results 651

Comparison of CH concentration predicted by GRI Mech and San Diego mechanisms 652  
for methane. 653

---

<sup>1</sup>In this notation, the letter represents the electronic energy level and the number in the parentheses represents the vibrational quantum number of the energy level

## CHAPTER 5

654

### LSB FLAME CHARACTERISTICS

655

In Chapter 2, we introduced the salient features of the Low Swirl Burner (LSB) flow field and discussed the mechanisms by which the LSB flame is stabilized. Further, various characteristics of the LSB flame that can be measured from flame images were outlined. To recapitulate, these are the flame location, flame shape and the flame structure. The first two are quantified by the flame standoff distance,  $X_f$ , and the flame angle,  $\theta_f$ , respectively.

In the same chapter, we introduced the four flow parameters that describe an operating condition for the LSB — the combustor pressure,  $p$ , the preheat temperature,  $T$ , the mass-averaged inlet velocity (also called the reference velocity,  $U_0$ ), and the equivalence ratio of the premixed reactants,  $\phi$ . We further introduced a geometric parameter — the angle of the vanes of the swirler,  $\alpha$ , which affects the amount of swirl present in the flow field.

The LSB flame was studied over a range of operating conditions, and the effect of flow and geometric parameters on the reacting flow field were investigated. The results of these investigations are presented in this chapter.

#### 5.1 Effect of reference velocity

671

In typical gas turbine applications, varying the loading on the engine does not affect the reference velocity. However, since the reference velocity is a design parameter, the effect it has on the flame characteristics has implications for the design of future LSB-based gas turbine engines.

One of the key objectives of this thesis is to investigate how the LSB flame stabilization operates at high pressure conditions. The simple model described in Chapter

FIXME 2 predicts a self-similar flow field for the LSB at all reference velocities. This implies that the reference velocity will have no discernible impact on the flame standoff distance. This result is desirable for gas turbine designers, since the flame location and shape can be assumed to be constant. Limited testing conducted in published works confirmed this behavior at atmospheric pressure conditions with no preheat.

In order to verify the validity of this model at high pressure conditions in the presence of substantial preheat, the LSB was operated at a pressure of 6 atm over a range of reference velocities from 10 m/s to 40 m/s. For these tests, the  $S_{37^\circ}$  swirler was used. In a parallel series of tests, the  $S_{45^\circ}$  swirler was tested at a pressure of 3 atm at a reference velocities of 40 and 80 m/s. The location of the flame was measured from CH\* chemiluminescence images, and the results are presented in Figure FIXME.

There is essentially no systematic variation in the flame standoff distance or the flame angle for the low velocity,  $S_{37^\circ}$  tests. Based on the model, this can be interpreted as the increase in reference velocity producing a concomitant increase in the turbulent flame speed at the flame stabilization location, negating any change in the flame's location. In other words, the flow field appears to retain its self-similarity, even at elevated pressures and temperatures.

When the  $S_{45^\circ}$  swirler was tested at higher reference velocities, however, the flame location shifted downstream sharply. This indicates potential limitations to the simple flame stabilization model that may not predict the behavior of the LSB flame at elevated pressures and temperatures, particularly at high reference velocities.

A possible cause of this limitation can be explored by considering the effect of increased reference velocity on the turbulent combustion regime in which the LSB combustor operates. Previous studies have primarily operated the LSB in the flamelet regime where the modified Damköhler model predicts the behavior of the turbulent flame speed with reasonable fidelity. At elevated pressures, both the laminar flame speed of the reactants,  $S_L$  and the flame thickness,  $\delta_f$  are diminished. This places

the operating regime higher and more to the right on a Borghi diagram, as shown in Figure FIXME. While increasing the reference velocity did not affect the turbulent combustion regime at lower pressures in a flamelet combustion regime, at elevated pressures the flame may be transitioning into the thin reaction zone regime. This transition would cause a reduction in  $S_T/S_L$ , or at least a lesser increase, and the turbulent flame speed would no longer be expected to increase in step with  $U_0$  and the increased levels of turbulence. This would explain the the observed downstream shift of the high pressure LSB flame at high reference velocities.

## 5.2 Effect of preheat temperature

The preheat temperature of the reactants is a key flow parameter, especially for gas turbine combustors. In general, the rates of most chemical reactions in the flame zone are highly sensitive to the temperature of the reactants. For the LSB in particular, the temperature of the incoming flow directly affects its viscosity and consequently, the velocity field in the flame stabilization region. Thus, studying the effect of the preheat temperature on the LSB flame and flow field is important.

In order to explore this in greater detail, the velocity field of the combustor was mapped using Laser Doppler Velocimetry (LDV). The conditions were chosen to study the effect of increasing the preheat temperature on both reacting and non-reacting LSB flow fields. Further, the study includes both low and high reference velocity cases. The relevant flow parameters relating to these tests are presented in Table FIXME. All LDV tests were limited to atmospheric pressure conditions. Implementing the LDV technique at elevated pressures proved difficult due to beam steering issues, coupled with impractical turn-around times between the successive runs that would be required to obtain sufficient LDV data points for analysis.

The normalized centerline mean and rms axial velocity profiles for the three cases are presented in Figure FIXME. The abscissa represents the distance from a point



called the virtual origin,  $X_0$ . The virtual origin is defined as the imaginary location where the extrapolated linear axial velocity profile reaches the reference velocity in magnitude. The extrapolation is indicated in Figure FIXME by a dashed line.

As noted in Chapter FIXME 2, previous studies[17] reported that mean axial stretch — the normalized slope of the linear decay of axial velocity — at the inlet of the combustor was self-similar, regardless of the Reynolds number,  $Re$  of the operating condition. Further, it was reported that the velocity decay was steeper for reacting cases compared to non-reacting cases.

The results presented in Figure FIXME however, show that even though Cases 1 and 2 have similar  $Re$ , their mean velocity profiles have very different slopes. Further, the reacting and non-reacting cases (both at preheated conditions) have similarly steep slopes. This indicates that the mean axial stretch in the near field of the LSB flow field is a stronger function of the preheat temperature than  $Re$ . The presence of preheat results in increased viscosity that enhances the momentum transport in the radial direction. This causes the velocity decay to be steep for preheated cases, compared to cases without preheat.

Assuming that  $S_T$  is constant, these results suggest that at higher preheat temperatures, the flame would stabilize closer to the dump plane because of the faster velocity decay and reduced local flow velocities. In fact, a faster velocity decay would produce greater  $u'$  values and increase  $S_T$ , further causing the flame location to shift upstream. Furthermore, in view of the steep velocity profile, it may be anticipated that any changes in the stabilization location caused by perturbations in the local flow field (and hence, the local turbulent flame propagation velocity) are likely to be of diminished magnitude in the presence of preheat. All of this leads to an intuitive result — the LSB flame behaves more stably at high preheat conditions.

### 5.3 Effect of swirler vane angle

756

As described in Chapter FIXME 3, the LSB swirlers tested for this study are designed to have the same mass flow splits. The  $S_{45^\circ}$  swirler has a higher vane angle, resulting in greater blockage to the flow passing through the annular section. In order to compensate for this, the perforated plate covering the central section has slightly smaller holes. The net effect retains the same mass flow split as in the  $S_{37^\circ}$  swirler.

Chapter FIXME 2 describes how the swirler vane angle relates to the amount of swirl imparted to the incoming flow. According to Equation FIXME, a swirler with a higher vane angle will produce greater swirl in the reactants. Previous work in swirl combustion[18, 19] has pointed out that increased swirl shortens the flame by enhancing the swirl-induced radial pressure gradients. The data acquired in the present investigation is in agreement with this observation. Operated at identical inlet conditions, the  $S_{45^\circ}$  swirler stabilizes a flame closer to the dump plane and with a larger flame angle compared to the  $S_{37^\circ}$  swirler.

This result highlights an interesting trade-off for the designers of LSB-based gas turbine engines. The  $S_{45^\circ}$  flame is located further upstream and has a more concentrated region of heat release. This enhances the strength of the toroidal recirculation zone near the dump plane, which may be powerful enough under certain conditions (as we shall see in Section 5.4) to even cause the flame to attach itself to the lip of the inlet. All of this means that the  $S_{45^\circ}$  flame is more stable and will resist perturbations in the incoming flow better than the  $S_{37^\circ}$  flame. However, the presence of a strong recirculation zone in the flow field of the  $S_{45^\circ}$  swirler will entrain more hot products and retain them longer near the zone of heat release. This is a recipe for the production of thermal  $\text{NO}_x$ . While no emission measurements were made as part of this study, it may be reasonably anticipated that the  $\text{NO}_x$  performance of the  $S_{45^\circ}$  swirler will be degraded compared to the  $S_{37^\circ}$  swirler. The trade-off for gas turbine

engine designers is thus between flame stability and emissions performance.

#### 5.4 Effect of equivalence ratio

The LSB is primarily intended for fuel-lean operation in order to utilize its low  $\text{NO}_x$  emission performance. As a result, most of the testing was done as close as possible to a target  $\phi$  of 0.56. Limited testing was carried out at 12 atm for two off-target conditions: a slightly richer ( $\phi \approx 0.58$ ) and a slightly leaner ( $\phi \approx 0.53$ ) mixture, in order to explore the sensitivity of the LSB flame to limited changes in equivalence ratio. The  $S_{45^\circ}$  swirler was used for these tests. The corresponding averaged and Abel-deconvoluted flame images are presented in Figure FIXME.

Two characteristics of the flame are immediately obvious from these images. First, the zone of heat release, marked by the region from which  $\text{CH}^*$  chemiluminescence is observed, is increasingly compact at fuel-rich conditions. Virtually all other flame images acquired at a leaner condition show a long flame, with the heat release distributed over the entire visible area of the combustor. The compactness of the heat release zone indicates potentially poor  $\text{NO}_x$  performance at these conditions.

Second, the fuel-rich flame brush can be observed to wrap around and anchor itself on the dump plane. This is particularly observable in the Abel-deconvoluted image. The attached region is not as bright as the rest of the flame brush, indicating that the flame may be attaching itself intermittently. This intermittent behavior can be confirmed from the instantaneous images where it is visible on some of the acquired images, but not others. This behavior was alluded to in Section 5.3 as being the result of the enhanced toroidal recirculation zone produced by this swirler. Thus, the intermittent attachment of the flame to the inlet indicates the increased importance of the toroidal recirculation zone in stabilizing the flame.

It should be noted that the reliance on a toroidal recirculation zone to anchor the flame to the inlet is one of the primary flame stabilization mechanisms used by

traditional swirl combustors. Thus, LSB swirlers with high vane angles tend to behave  
like traditional swirl combustors at fuel-rich conditions.

## 5.5 Effect of combustor pressure

In many gas turbine engines, the combustor pressure varies directly with the loading  
of the engine. Like the preheat temperature, the combustor pressure affects the LSB  
flame both through the fluid mechanics of the flow and the kinetics of the chemical  
reactions in the flame. The effect of the combustor pressure on the fluid mechanics  
of the LSB flow field can be captured by its effect on the Reynolds number. As noted  
in Section 5.2, however, previous work indicated the Reynolds number may not be  
an important parameter for the LSB, particularly in the near field where the flame  
stabilization occurs. On the other hand, the effect of the combustor pressure on reac-  
tion rates in the flame is clearly important. Increasing the combustor pressure results  
in a lower laminar flame speed and reduced flame thickness for methane-air flames.  
According to the modified Damköhler model discussed earlier, the reduced laminar  
flame speed should have little or no effect on the flow field, since the contribution from  
 $S_L$  in Equation FIXME is vanishingly small, even at the lowest reference velocities  
of our test conditions. However, as suggested by our discussion in Section 5.1, the  
validity of the simple model at elevated pressure conditions is questionable.

In order to resolve the uncertainties regarding how the LSB flame responds to  
combustor pressure, the flame was imaged over a range of operating conditions from  
3 to 12 atm. For these tests, the reference velocity and the equivalence ratio were  
held constant. However, the temperature of the reactants continues to increase with  
pressure. The reason for this was discussed in Chapter FIXME 3 and is attributable  
to the reduced heat losses in the connecting pipes at the high flow rates required to  
pressurize the LSB. The flame location and shape inferred from the flame images are  
presented in Figure FIXME.

At low to moderate pressures, the flame location is nearly invariant for  $S_{37^\circ}$ , but  
 moves upstream for the  $S_{45^\circ}$  cases. This behavior can be explained as follows. The  
 flame stabilization location for the  $S_{45^\circ}$  swirler is closer to the dump plane compared  
 to the  $S_{37^\circ}$  swirler. This should result in enhanced heat transfer to the dump plane  
 and consequently to the incoming reactants. This feedback is even more effective as  
 the temperature of the incoming reactants increases. This causes the upstream shift  
 of the  $S_{45^\circ}$  flame, while the  $S_{37^\circ}$  flame is less affected by these processes.

At high pressures, however, both flames are observed to move downstream, despite  
 the increasing preheat temperatures. The apparent decrease in the turbulent flame  
 speed at these conditions is an unexpected result, and the modified Damköhler model  
 is insufficient in accounting for this observation. Figure FIXME also shows that the  
 flame angle for both cases decreases slightly with pressure. This suggests that the  
 turbulent flame speed was consistently decreasing with pressure. In light of this,  
 the nearly constant location of the  $S_{37^\circ}$  flame could be attributed to the effects of  
 increasing combustor pressure and preheat temperature nearly canceling each other  
 out at the lower pressures.

## 5.6 Flame structure

**CHAPTER 6**  
**CONCLUSIONS**

851

852

## APPENDIX A

853

### SEEDER DESIGN

854

A new seeder was designed for use in high pressure implementations of diagnostic techniques like Laser Doppler Velocimetry (LDV), Particle Image Velocimetry (PIV), etc.

The previous design, as shown in Figure A.1, was a fluidized bed seeding generator. Seeding particles in a cylindrical vessel are fluidized by an air-turbine vibrator. Air is introduced into the vessel in the form of two opposing jets directed tangentially to produce a small amount of swirl in the flow field. Particles are picked up by the air flow and the swirl aids in separating the heavy/coagulated clumps of seeding particles by centrifugal acceleration.

This design had several shortcomings. First, it is observed that the seeding density of the seeded flow generally decreases over time, even if the seeding particles have not been depleted. The seeding particles tend to coagulate over time, due to the buildup of moisture, static charge, etc. In such cases, the vibrator can no longer effectively fluidize the particles. Further, the tangential introduction of the air flow preferentially depletes particles near the walls of the container, leaving the center relatively undisturbed. The cumulative effect of these phenomena diminishes the effectiveness of the seeder.

Second, the fluidized bed requires a minimum amount of seeding particles to function effectively. This requires the seeder to be refilled even before all the seeding particles are consumed.

Third, when designed for high pressure applications, the seeder will become quite heavy due to flanges and other fittings. Such a setup cannot be easily fluidized using a reasonable-sized air-turbine vibrator.

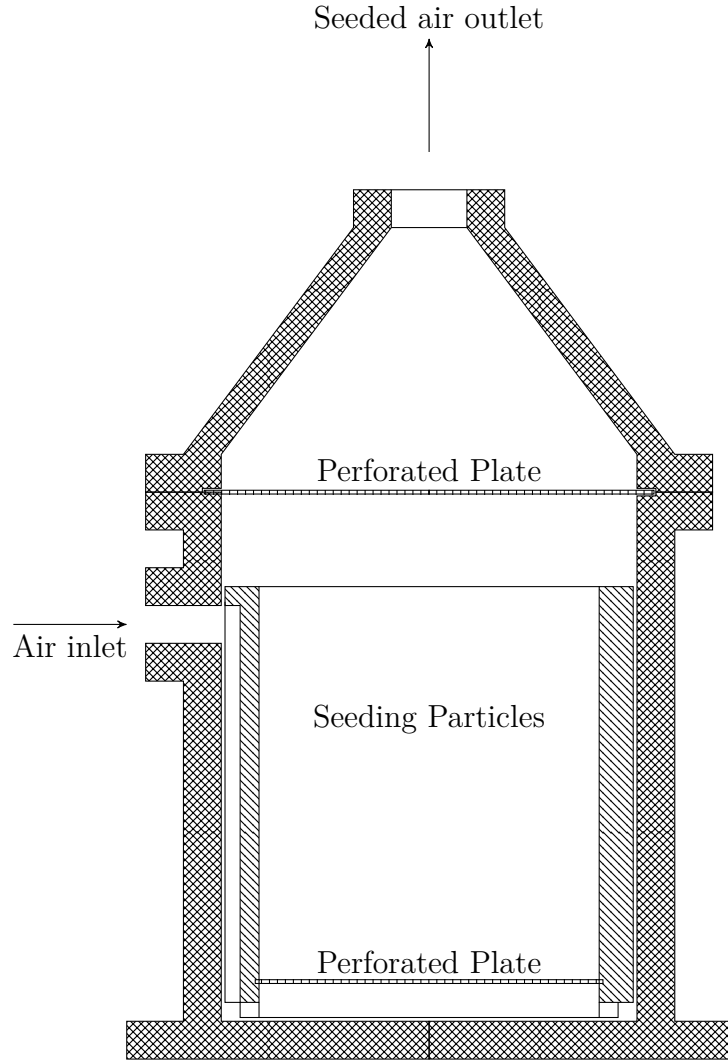


Figure A.1: A schematic of the old fluidized bed seeder is presented. The air enters the seeder through a groove along the inner vessel and is injected with a tangential velocity at the base of the seeder. The whole assembly is vibrated (vibrator not shown) to keep the particle bed fluidized. The seeded air flow exits through the outlet on the top.



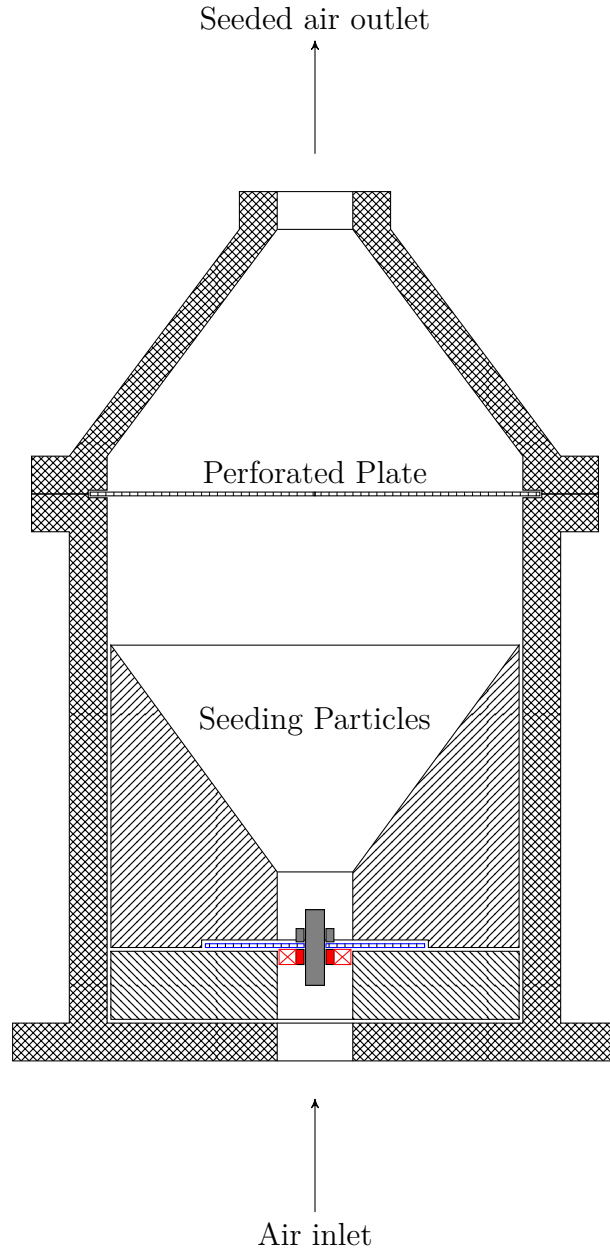


Figure A.2: *The improved design of the seeder is shown here in schematic form. The air enters the assembly from the inlet at the bottom, passes through the swirler (shown in red) and enters the seeder. The perforated plate at the bottom (shown in blue) keeps the seeding particles within the seeder. The swirler hub is threaded, allowing it to be secured to the perforated plate by a short steel bolt (shown in gray). After picking up the particles, a second perforated plate prevents large clumped seeding particles from passing through. The seeded air flow exits through the outlet at the top.*

The new seeder design is shown in Figure A.2, and resembles a funnel with a 878  
swirler located halfway up the stem. A perforated base plate holds the swirler and 879  
the seeding particles in the conical section of the swirler. Due to the steep angle of the 880  
sides of the conical section, the seeding particles continuously collapse into the central 881  
section. This negates any need for vibrating the system. Air is introduced from the 882  
bottom of the seeder and enters the vessel by passing through the swirler. Since all 883  
the air enters this way, there is a considerable amount of swirl in the resulting flow 884  
field, Heavy/coagulated seeding particles are flung outward, while lighter particles are 885  
carried with the air. After a sufficient distance to allow for the cyclonic separation 886  
to be effective, the seeded air passes through another perforated plate which further 887  
limits the presence of large clumps of particles. The exiting air is now spatially and 888  
temporally uniformly seeded. 889

## REFERENCES

- [1] N. L. Garland and D. R. Crosley, "Relative transition probability measurements  
in the  $A - X$  and  $B - X$  systems of CH," *Journal of Quantitative Spectroscopy  
and Radiative Transfer*, vol. 33, no. 6, pp. 591–595, 1985.
- [2] J. Luque and D. R. Crosley, "Electronic transition moment and rotational tran-  
sition probabilities in CH. I.  $A^2\Delta - X^2\Pi$  system," *Journal of Chemical Physics*,  
vol. 104, no. 6, pp. 2146–2155, 1996.
- [3] G. Richmond, M. L. Costen, and K. G. McKendrick, "Collision-Partner Depen-  
dence of Energy Transfer between the CH  $A^2\Delta$  and  $B^2\Sigma^-$  States," *The Journal  
of Physical Chemistry A*, vol. 109, no. 4, pp. 542–553, 2005.
- [4] T. A. Cool and P. J. H. Tjossem, "Direct observations of chemi-ionization in hy-  
drocarbon flames enhanced by laser excited  $\text{CH}^*(A^2\Delta)$  and  $\text{CH}^*(B^2\Sigma^-)$ ," *Chem-  
ical Physics Letters*, vol. 111, no. 1-2, pp. 82–88, 1984.
- [5] N. L. Garland and D. R. Crosley, "Energy transfer processes in CH  $A^2\Delta$   
and  $B^2\Sigma^-$  in an atmospheric pressure flame," *Applied Optics*, vol. 24, no. 23,  
pp. 4229–4237, 1985.
- [6] J. Luque, R. J. H. Klein-Douwle, J. B. Jeffries, and D. R. Crosley, "Collisional  
processes near the CH  $B^2\Sigma^- v' = 0, 1$  predissociation limit in laser-induced fluo-  
rescence flame diagnostics," *Applied Physics B: Lasers and Optics*, vol. 71, no. 1,  
pp. 85–94, 2000.
- [7] C. Chen, Y. Sheng, S. Yu, and X. Ma, "Investigation of the collisional quenching  
of CH( $A^2\Delta$  and  $B^2\Sigma^-$ ) by Ar,  $\text{O}_2$ ,  $\text{CS}_2$ , alcohol, and halomethane molecules,"  
*The Journal of Chemical Physics*, vol. 101, no. 7, pp. 5727–5730, 1994.

- [8] M. Tamura, P. A. Berg, J. E. Harrington, J. Luque, J. B. Jeffries, G. P. Smith, and D. R. Crosley, “Collisional Quenching of CH(A), OH(A), and NO(A) in Low Pressure Hydrocarbon Flames,” *Combustion and Flame*, vol. 114, no. 3-4, pp. 502–514, 1998.
- [9] M. W. Renfro, K. K. Venkatesan, and N. M. Laurendeau, “Cross sections for quenching of CH  $A^2\Delta$ ,  $v' = 0$ , by N<sub>2</sub> and H<sub>2</sub>O from 1740 to 2160 K,” in *Proceedings of the Combustion Institute*, vol. 29, pp. 2695–2702, 2002.
- [10] J. Luque and D. R. Crosley, “Electronic transition moment and rotational transition probabilities in CH. II.  $B^2\Sigma^- - X^2\Pi$  system,” *Journal of Chemical Physics*, vol. 104, no. 11, pp. 3907–3913, 1996.
- [11] M. Zachwieja, “New Investigations of the  $A^2\Delta - X^2\Pi$  Band System in the CH Radical and a New Reduction of the Vibration-Rotation Spectrum of CH from the ATMOS Spectra,” *Journal of Molecular Spectroscopy*, vol. 170, no. 2, pp. 285–309, 1995.
- [12] D. T. Yegian and R. K. Cheng, “Development of a lean premixed low-swirl burner for low NO<sub>x</sub> practical applications,” *Combustion Science and Technology*, vol. 139, no. 1, pp. 207–227, 1998.
- [13] A. Marshall, P. Venkateswaran, D. Noble, J. Seitzman, and T. Lieuwen, “Development and characterization of a variable turbulence generation system,” *Experiments in Fluids*, vol. 51, no. 3, pp. 611–620, 2011.
- [14] A. Melling, “Tracer particles and seeding for particle image velocimetry,” *Measurement Science and Technology*, vol. 8, no. 1, pp. 1406–1416, 1997.
- [15] Y. Hardalupas, C. S. Panoutsos, and A. M. K. P. Taylor, “Heat Release Rate Measurements in Premixed Flames using Chemiluminescence and Reaction Rate

- Imaging,” in *44th AIAA Aerospace Sciences Meeting and Exhibit, Reno, NV, January 9–12, 2006.* 937  
938
- [16] C. J. Dasch, “One-dimensional tomography: a comparison of abel, onion-peeling, 939  
and filtered backprojection methods,” *Applied Optics*, vol. 31, no. 8, pp. 1146– 940  
1152, 1992. 941
- [17] R. K. Cheng, D. Littlejohn, W. A. Nazeer, and K. O. Smith, “Laboratory Studies 942  
of the Flow Field Characteristics of Low-Swirl Injectors for Adaptation to Fuel- 943  
Flexible Turbines,” *Journal of Engineering for Gas Turbines and Power*, vol. 130, 944  
p. 021501, 2008. 945
- [18] C. K. Chan, K. S. Lau, W. K. Chin, and R. K. Cheng, “Freely propagating open 946  
premixed turbulent flames stabilized by swirl,” in *Symposium (International) on 947  
Combustion*, vol. 24, pp. 511–518, 1992. 948
- [19] S. H. Stårner and R. W. Bilger, “Joint measurements of velocity and scalars in 949  
turbulent diffusion flame with moderate swirl,” in *Symposium (International) on 950  
Combustion*, vol. 21, pp. 1569–1577, 1986. 951